

Annihilation of Weyl nodes in the Extreme Quantum Limit of TaAs

B. J. Ramshaw,^{1,2*} K. A. Modic,³ Arkady Shekhter,³ Philip J. W. Moll,⁴
M. K. Chan,² J. B. Betts,² F. Balakirev,² A. Migliori,² N. J. Ghimire,⁵
E. D. Bauer,² F. Ronning,² R. D. McDonald.²

¹Present address: Laboratory of Atomic and Solid State Physics, Cornell University, Ithaca, NY, 14853.

²Los Alamos National Laboratory, Los Alamos, New Mexico, 87545.

³Max-Planck-Institute for Chemical Physics of Solids, Noethnitzer Strasse 40.

⁴National High Magnetic Field Laboratory, Tallahassee, Florida, 32310.

⁵Materials Science Division, Argonne National Laboratory.

*To whom correspondence should be addressed; E-mail: bradramshaw@cornell.edu.

Extreme magnetic fields confine electrons in a metal to a single highly degenerate quantum level—a regime known as the quantum limit. As nature abhors degeneracy, this regime is unstable to the formation of new states of matter, such as the fractional quantum Hall state in two spatial dimensions. The fate of three-dimensional metals in the quantum limit, on the other hand, has remained largely unexplored. We use 95 tesla magnetic fields to take the Weyl semimetal TaAs deep into its quantum limit, where the electronic properties are determined by the $n = 0$ Landau levels alone. In this limit we find magnetic-field-independent conductivity when the electric current is parallel to the magnetic field up to 50 tesla—a clear demonstration of the Adler-Bell-Jackiw anomaly for Weyl Fermions. Above 50 tesla the cyclotron energy ex-

ceeds the intrinsic spin-orbit interaction strength in TaAs and we observe the annihilation of the Weyl nodes and subsequent loss of the ABJ-induced conductivity. Loss of the Weyl points and increased degeneracy induce a sharp thermodynamic phase transition that we observe at the highest magnetic fields, indicating that electron-electron interactions can induce new phases of matter in Weyl systems once topological protection is lifted.

The study of electron systems under intense magnetic fields has led to many fundamental breakthroughs in physics, including the integer and fractional quantum hall states (1, 2), the discovery of Dirac electrons in graphene (3), and quantum phase transitions in topological insulators (TIs) (4). These inherently quantum phenomena are revealed when the cyclotron energy induced by the magnetic field becomes large compared to the the Fermi energy (the intrinsic energy scale of a metal). Such discoveries have largely been confined to two-dimensional systems, where carrier densities can be tuned and the quantum limit can be kept within the bounds of magnetic fields available in the laboratory. An analogous experiment in a typical three dimensional metal such as copper, for example, would require magnetic fields greater than 60,000 tesla (currently only available on the surfaces of neutron stars (5)). Semimetals with low carrier densities, on the other hand, bring the possibility of reaching quantum degeneracy within reach of the highest available magnetic fields (6–8).

Weyl semimetals combine low carrier densities with linear energy-momentum dispersions near a point where two bands cross—somewhat analogous to graphene but in three dimensions (9, 10). An important further twist in the electronic structure of Weyl semimetals is the presence of a broken symmetry (inversion or time-reversal) and strong spin-orbit coupling that lifts degeneracy between spin up and spin down carriers. This separates the energy bands into two separate Dirac spectra of opposite chirality—each band crossing a source or sink of Berry flux known as a Weyl point (11). There are three outstanding issues in Weyl systems that we

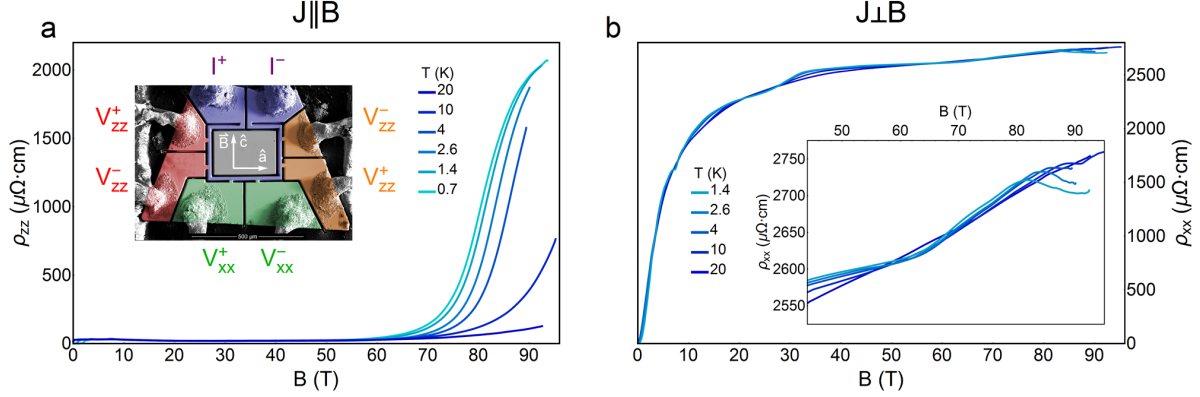


Figure 1: **Magnetoresistance TaAs up to 95 tesla.** **a**, Resistivity for $\vec{J}||\vec{B}||\hat{c}$ at temperatures ranging from 0.7 to 20 K. The inset shows the single-crystal of TaAs that was microstructured using focused-ion-beam lithography for both ρ_{zz} and ρ_{xx} measurements. The low field data is shown in detail in Figure 2. **b**, Resistivity for $\vec{J}\perp(\vec{B}||\hat{c})$ in the same sample (no ρ_{xx} data was obtained for $T = 0.7$ K, all other temperatures are the same). The inset highlights the structure of the high-field data.

address with high magnetic fields: the first is whether the anomalous Adler-Bell-Jackiw (ABJ) contribution to the conductivity can be observed in the quantum-limit; the second is the fate of the topologically-protected Weyl points (12) when the magnetic field is stronger than the spin orbit interaction; and the third is the possibility of an electron-electron interaction driven instability in the highly degenerate quantum limit (13).

Figure 1 shows the resistivity of the Weyl semimetal TaAs in magnetic fields up to 95 tesla for. We used focused-ion beam lithography (FIB) to microstructure a single-crystal sample such that both ρ_{xx} and ρ_{zz} can be measured simultaneously, and to carefully define the current path and voltage contacts (see S.I. for a discussion of negative magnetoresistance in these samples). Immediately striking is the two-order-of-magnitude increase in resistance that onsets above 50 tesla for the current and field configuration $\vec{J}||\vec{B}||\hat{c}$ (Figure 1a). ρ_{zz} is strongly temperature dependent at high fields, exhibiting activation with a characteristic energy scale that increases with field at a rate of 1.3 kelvin/tesla (see S.I.). The resistivity in the $\vec{J}\perp(\vec{B}||\hat{c})$ configuration, on the other hand, exhibits strong magnetoresistance at low fields as expected when current flows

perpendicular to the magnetic field, but shows no such temperature-dependent increase at 50 tesla (Figure 1b). As we will discuss below, the low resistivity of ρ_{zz} followed by the sudden upturn at 50 tesla (and the lack of such a feature in ρ_{xx}) is related to the anomalous conductivity provided by the $n = 0$ Landau levels (LLs) of the Weyl Fermions.

In order to understand the features in the resistivity we must first understand how the underlying bands in a Weyl semimetal evolve with magnetic field. The electronic structure of TaAs has been shown to contain two sets of electron-like carriers with topologically protected Weyl Fermions, and hole-like carriers with a trivial parabolic spectrum (see Figure 2c) (14–16)—our own quantum oscillation frequencies agree with those reported earlier. In a magnetic field the electronic spectra for both carrier types are quantized into LLs with quantum numbers $n = 0, 1, 2, 3, \dots$. There is an important distinction between carriers characterized by trivial (parabolic) or Dirac spectra: the energy spectrum of the $n = 0$ LL for Dirac carriers is field-independent and disperses linearly in k_z (momentum along the direction of \vec{B}), whereas the energy of the $n = 0$ LL of parabolic carriers is field-dependent and disperses quadratically in k_z . The distinct behaviours of the two carrier types in a magnetic field are profoundly different in the quantum limit (2c) (17). In addition to linear dispersions, Weyl semimetals have broken spin degeneracy. As a result the $n = 0$ LLs of the two carrier chiralities are separated in the Brillouin zone, with one chirality dispersing as k_z and the other as $-k_z$. Physically each of the two 0th LLs of the Weyl Fermions can be thought of as containing carriers that only propagate along a single direction—parallel to \vec{B} for one chirality (“up movers”), and anti-parallel for the other (“down movers”). This separation of the two carrier chiralities in momentum space gives rise to the anomalously high conductivity predicted to occur in Weyl semimetals for $\vec{B} \parallel \vec{J}$: for “up movers” to scatter and become “down movers” (the source of resistance in a metal) they must scatter to the other Weyl node. This scattering probability is suppressed because of the highly constrained momentum transfer and change in chirality between the two nodes, and the

conductivity is therefore anomalously large along the k_z direction. The notion of a “chiral anomaly” in this context comes from the population imbalance between two carrier chiralities when the electric field (current) is parallel to the magnetic field, analogous to the ABJ anomaly in field theory (9).

Previous studies have focused on the anomalous conductivity when the magnetic field is much lower than the quantum limit ($B \ll B_{QL}$, where B_{QL} is the “quantum limit” (QL)), where it is expected to manifest as negative magnetoresistance—resistance that drops with increasing magnetic field (18). These studies are inconclusive, however, in part because there are other effects that can give rise to negative magnetoresistance (19–21). Here we instead focus on the conductivity at high fields; all measurements were performed with the magnetic field aligned with the crystal \hat{c} axis to provide the lowest quantum limit for the Weyl pockets. Figure 2 shows quantum oscillation in ρ_{xx} and ρ_{zz} up to 7.5 Tesla—the QL of the electron Weyl pockets (16). The trivial hole pocket also shows quantum oscillations (clearest in ρ_{xx}) and enters the quantum limit (all carriers in the $n = 0$ LL) at 18 T (16). The ultimate location of the chemical potential in the quantum limit depends on the net carrier number, which is electron-like for TaAs (see S.I. and also Huang *et al.*, Zhang *et al.*, and Arnold *et al.* (14–16)). This determines that the chemical potential remains in the electron-like Weyl pockets and that the hole pocket is completely depleted in high fields at roughly $2 \times B_{QL}$ of the holes or 36 tesla (see Figure 3b). We observe a final oscillation in ρ_{xx} at 36 tesla when the $n = 0$ LL of the hole pocket passes through the chemical potential. With the hole pocket depleted the only states contributing to the conductivity above 36 tesla are the $n = 0$ LLs from the Weyl pockets. Even before the hole pocket is completely depleted the high mobility $n = 0$ Weyl electrons dominate the electrical transport and ρ_{zz} becomes nearly field and temperature independent above approximately 25 tesla (Figure 2). This field-independent behaviour of ρ_{zz} has been predicted for the conductivity when only the $n = 0$ LLs of the Weyl carriers are occupied (9, 18), and is a direct

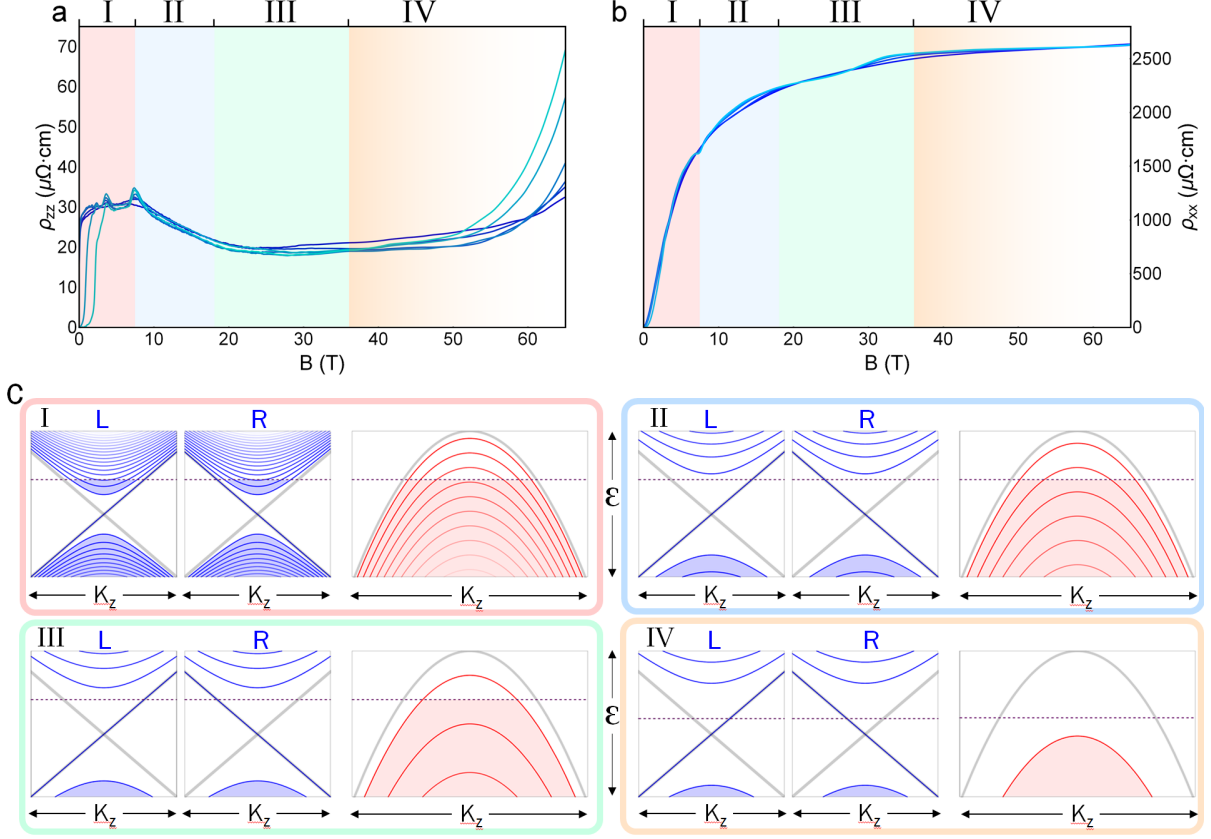


Figure 2: The four distinct regimes of Landau level occupancy in TaAs up to 65 tesla. TaAs hosts two pairs of Weyl nodes with similar quantum limits for this field orientation; one pair of Weyl pockets is shown here along with the trivial hole pocket. **a,b**, Resistivity of TaAs at temperatures between 0.7 K and 20 K, for $\vec{J} \parallel \vec{B} \parallel \hat{c}$ (**a**) and for $\vec{J} \perp (\vec{B} \parallel \hat{c})$ (**b**), from 0 to 65 Tesla. **c**, Schematic of the Landau level (LL) structure and occupancy for the parabolic hole pockets (red lines) and Weyl electron pockets (blue lines). Region **I** is from 0 to 7.5 tesla, where both hole and electron pockets exhibit quantum oscillations. Between 7.5 and 18 Tesla (region **II**) the electron pockets are in their $n = 0$ LL, whereas the hole pocket is still in its $n = 1$ LL. Between 18 and 36 Tesla (region **III**) the hole pocket is also in its $n = 0$ LL. At 36 tesla the last oscillation corresponding to emptying the $n = 0$ LL of the hole pocket occurs. Above 36 tesla (region **IV**) the only occupied states at the chemical potential are in the $n = 0$ LL of the Weyl electron pockets, and the chemical potential shifts to maintain charge neutrality. The fading in region **IV** represents the breakdown of the separate Weyl node picture when $\hbar\omega_c$ exceeds the spin orbit interaction.

demonstration of the ABJ anomaly in the conductivity of a Weyl semimetal.

Having established the quantum-limit transport properties of TaAs at intermediate fields we turn to higher fields where the cyclotron energy becomes comparable to the spin-orbit interaction strength. Above 50 tesla we observe a large increase in ρ_{zz} with increasing magnetic field that exhibits an activated temperature dependence (Figure 1a). We interpret this departure from the constant conductivity at lower fields as an indication of the merger of the two Weyl nodes and subsequent loss of the ABJ-induced conductivity. The spin-orbit splitting of the quasiparticle bands in TaAs that results in separate Weyl nodes is between 50 and 100 meV (16). By 50 tesla the cyclotron energy, $\hbar\tilde{\omega}_c = \hbar\sqrt{\frac{2eB}{\hbar}}v_F$, is 80 meV and thus exceeds the strength of the spin-orbit interaction. While the Weyl nodes are topologically protected from small perturbations, a cyclotron energy of 80 meV is not perturbative. A schematic for one possible method by which this leads to the annihilation of the Weyl nodes and the loss of ABJ anomaly-induced conductivity is shown in Figure 3. We stress that because spin-orbit interactions do not commute with magnetic field Figure 3 is only schematic: the usual semi-classical procedure of superimposing LLs (e.g. those shown in Figure 2c) on the zero-field bandstructure fails when the LL spacing is larger than the spin-orbit splitting. A quantitative description of exactly how the LLs evolve under these conditions—and exactly how the Weyl nodes are annihilated in high fields—is an unresolved question for Weyl semimetals and is an important direction for future theoretical studies. Note that we do not observe a similar increase in ρ_{xx} above 50 tesla: this is because there is no anomalous contribution to the conductivity for $\vec{B} \perp \vec{J}$, and so the merger and subsequent annihilation of the Weyl nodes does not affect the conductivity in this direction. The rollover in ρ_{xx} above 30 tesla indicates a conductance contribution from the surface of the sample (see S.I.). This either originates from the topological surface states, which have been observed with surface-sensitive measurements (22, 23), or from an amorphous layer created by the FIB process (24).

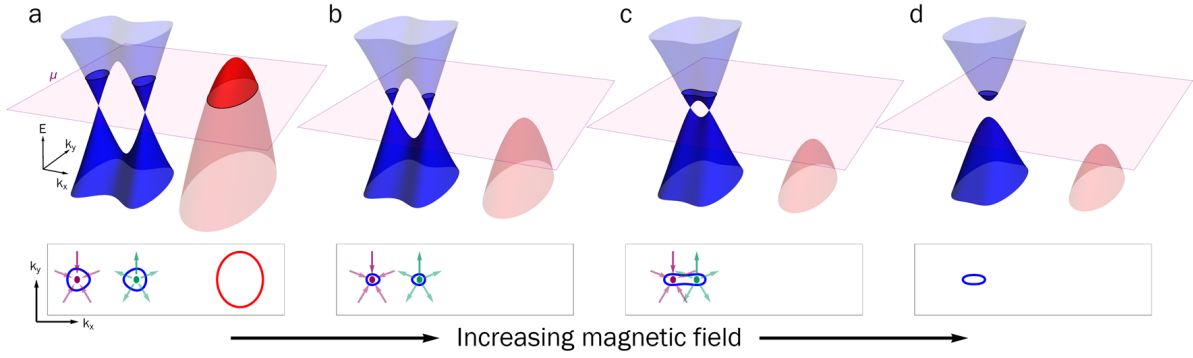


Figure 3: Annihilation of the Weyl nodes. A schematic bandstructure containing electron-like Weyl pockets (blue) and a hole-like trivial pocket (red). Not shown are a second set of electron-like Weyl pockets also present in TaAs (16). **a**, A two-dimensional slice of the bandstructure (along $k_z = 0$) at zero magnetic field. The top panels show the energy-momentum dispersion; bottom panels show the Fermi cross section and the two sources of Berry flux (green and purple arrows) at the Weyl nodes (green and purple points). **b**, Above 36 Tesla the hole pocket is entirely gapped out and the chemical potential moves toward the Weyl nodes, reducing the Weyl Fermi volume such that the net carrier density remains constant. **c**, In a sufficiently high magnetic field Zeeman coupling of the bands can bring the Weyl nodes together (the inverted bands pull apart). With the chemical potential above the Weyl nodes the two Fermi pockets can merge into a single pocket before the Weyl points themselves merge, leading to a loss of the protected ABJ conductivity. **d**, Beyond a threshold field the Weyl nodes merge in momentum space and annihilate, leaving behind a low density semimetal.

As the magnetic field increases so too does the LL degeneracy, making the system unstable to the formation of a new interaction-driven state (25). At 80 tesla we see a sharp decrease in ρ_{xx} at the lowest temperature (inset of Figure 1b): such features are generally indicative of a phase transition. To investigate this possibility further we measured the longitudinal sound velocity (v_{zz}) of TaAs using pulse echo ultrasound up to 95 tesla (see S.I. for experiment details), providing a thermodynamic probe into the physics at the highest fields (Figure 4). There are two main features of note in the sound velocity: a broad minimum centered around 65 tesla that disappears with increasing temperature, and a strong increase in sound velocity above 80 tesla at the lowest two temperatures. The dip coincides with a similar feature in ρ_{xx} , and resembles a quantum oscillation. This is a second consequence of the strong magnetic fields: as the cyclotron energy exceeds the spin-orbit interaction the two chiralities mix together (because magnetic field and spin orbit do not commute), allowing for the formation of new cyclotron orbits around the Fermi surface (see Figure 3c)¹. Thus the appearance of a quantum oscillation-like feature near 50 tesla is consistent with the loss of the ABJ anomaly observed in ρ_{zz} at the same field. Note that while both ρ_{xx} and the sound velocity (described below) show a feature that is symmetric about 65 tesla, the increase in ρ_{zz} is monotonic and thus qualitatively different from a quantum oscillation.

At the lowest temperatures (below 2.5 K) we observe a sudden increase in sound velocity above 80 tesla, accompanied by a strong increase in ultrasonic attenuation (Figure 4). The onset of this behaviour coincides in magnetic field with the sharp decrease in ρ_{xx} , and we take all three phenomena as evidence for a field-induced phase transition. No discontinuity in ρ_{zz} —obtained in the same sample as the ρ_{xx} data—is visible at this field: it would appear that the loss of the

¹A simple picture for this is magnetic breakdown between the separate Weyl pockets. In the limit of $\hbar\omega_c \ll E_F$ the probability of magnetic breakdown occurring for any given quasiparticle orbit is $P = e^{-\frac{\Delta^2}{\hbar\omega_c E_F}}$, where E_F is the Fermi energy and Δ is the gap separating two cyclotron orbits (26). In the case of TaAs above 50 tesla, $\hbar\omega_c \gg E_F$ and so this simple picture is obviously incomplete.

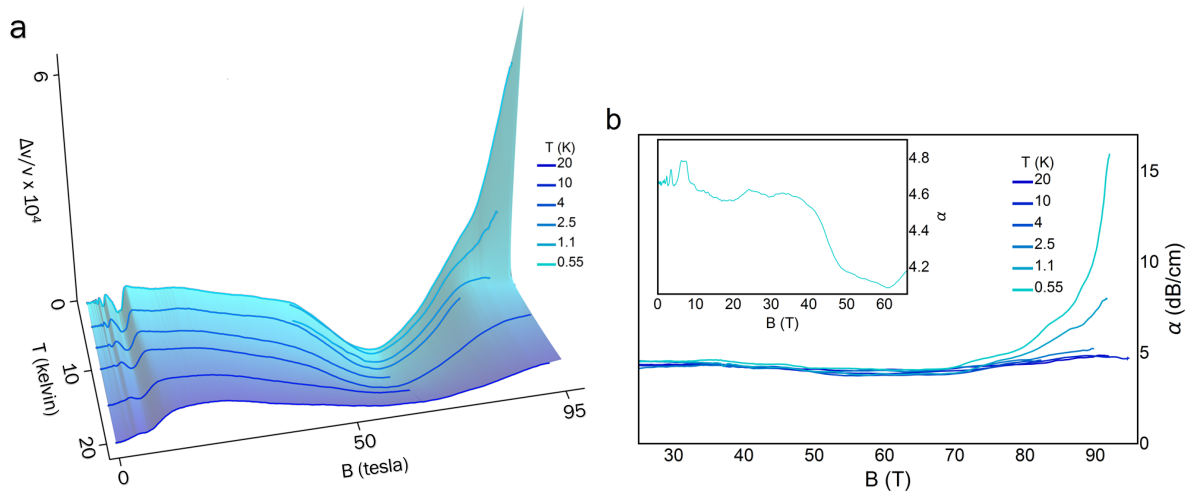


Figure 4: **Speed of sound and ultrasonic attenuation in TaAs.** **a**, Change in the speed of 315 MHz ultrasound for $\vec{k} \parallel \vec{B} \parallel \hat{c}$, where \vec{k} is the propagation wavevector of the longitudinal (compressional) sound. Data from two different experiments—one from 0 to 65 tesla and one from 45 to 95 tesla—are combined in this plot. **b**, The ultrasonic attenuation for the same sound and field configuration as **a**, with data from 0 to 65 tesla shown in the inset. Above 2.5 K the sound velocity flattens out above 80 tesla and the attenuation is only weakly field dependent. Below 2.5 K, however, both the sound velocity and the ultrasonic attenuation increase rapidly with field.

ABJ anomaly overwhelms any change in ρ_{zz} that might be attributed to the phase transition itself.

When the magnetic field is sufficiently strong such that scattering between LLs is energetically prohibited the quasiparticles are confined to move only along k_z . This effectively confines the electronic system to one dimension, where electron-electron interactions favour the formation of a broken symmetry state such as a Peierls-type density wave. Such an instability is thought to occur in the quantum limit of graphite, where a series of phase transitions are observed as a function of magnetic field as the last few LLs are depopulated (6–8). The activated temperature dependence of the conductivity in TaAs for $\vec{J}||\vec{B}||\hat{c}$ and corresponding weak response for $\vec{J}\perp(\vec{B}||\hat{c})$ is remarkably similar to what is observed in graphite. This may indicate a gap opening from the merger of the Weyl nodes (Figure 3d), followed by a second, interaction-driven transition at 80 tesla. Further evidence for a phase transition at 80 tesla comes from the ultrasonic attenuation. When the wavelength of sound is much longer than the quasiparticle mean free path the attenuation α is proportional to the electrical conductivity (27). The attenuation and ρ_{zz} of TaAs track each other in this way from the low-field oscillatory behaviour up to the rise in ρ_{zz} at 50 tesla, but above 80 tesla the attenuation increases dramatically while the conductivity *decreases*. This suggests that the dominant mechanism of attenuation at high fields is not the direct interaction between ultrasound and the conduction electrons, but is instead the response of ultrasound to order parameter fluctuations near the phase transition.

The measurements we present here demonstrate that TaAs exhibits the topologically-protected ABJ conductivity predicted for Weyl Fermions deep in the quantum limit, and that the Weyl nodes are eventually annihilated in high magnetic fields. This represents a new regime for the study of Weyl semimetals and requires a deeper theoretical understanding of how the single-particle energy levels in a Weyl system evolve when the Fermi energy, the cyclotron energy, and the spin-orbit interaction are all comparable in energy. We further observe a phase transition at

80 tesla that is indicative of an instability to the formation of a new state of matter in the quantum limit, likely an inherently many-body state in analogy with those that form in the quantum limit of a 2D electron gas (25). For comparison, graphene is also unstable to the formation of new states when only the $n = 0$ LL is occupied in high magnetic fields (12, 28). Depending on competing energy scales, including disorder and the in-plane magnetic field component, possible ground states for graphene in high magnetic fields include charge and spin density waves, quantum spin Hall states (also observed in the $n = 0$ LL of the 2D surface states in HgTe quantum wells (4)), and topological states that undergo a Kosterlitz-Thouless transition (12, 29, 30). It has long been proposed that in sufficiently high magnetic fields three dimensional metals can also undergo collective transitions to new states of matter such as Wigner crystals, fractional states, excitonic insulators, charge and spin density waves, and other possibilities (13). While we are unable to identify the exact nature of the high field state in TaAs with our present measurements, our ability to observe the transition in a thermodynamic quantity—sound velocity—is a promising step forward that is unavailable for most 2D electron systems and which has eluded observation at the field-induced transitions in graphite (31).

References

1. K. v. Klitzing, G. Dorda, M. Pepper, *Phys. Rev. Lett.* **45**, 494 (1980).
2. D. C. Tsui, H. L. Stormer, A. C. Gossard, *Phys. Rev. Lett.* **48**, 1559 (1982).
3. K. S. Novoselov, *et al.*, *science* **306**, 666 (2004).
4. M. König, *et al.*, *Science* **318**, 766 (2007).
5. C. Thompson, R. Duncan, *Astrophysical Journal* **408**, 194 (1993).
6. S. Tanuma, *et al.*, *Springer Series in Solid State Sciences* (1981).

7. B. Fauqué, *et al.*, *Phys. Rev. Lett.* **110**, 266601 (2013).
8. Z. Zhu, *et al.*, *arXiv preprint arXiv:1508.03645* (2015).
9. H. B. Nielsen, M. Ninomiya, *Physics Letters B* **130**, 389 (1983).
10. G. W. Semenoff, *Phys. Rev. Lett.* **53**, 2449 (1984).
11. T. Wehling, A. M. Black-Schaffer, A. V. Balatsky, *Advances in Physics* **63**, 1 (2014).
12. S. M. Young, *et al.*, *Phys. Rev. Lett.* **108**, 140405 (2012).
13. B. I. Halperin, *Proc. 18th Int. Conf. on Low Temperature Physics* **26** (1987).
14. X. Huang, *et al.*, *Phys. Rev. X* **5**, 031023 (2015).
15. C.-L. Zhang, *et al.*, *Nature Communications* **7** (2016).
16. F. Arnold, *et al.*, *Phys. Rev. Lett.* **117**, 146401 (2016).
17. P. J. W. Moll, *et al.*, *Nature Communications* **7** (2016).
18. B. Z. Spivak, A. V. Andreev, *Phys. Rev. B* **93**, 085107 (2016).
19. A. B. Pippard, *Magnetoresistance in metals*, vol. 2 (Cambridge University Press, 1989).
20. R. D. dos Reis, *et al.*, *New Journal of Physics* **18** (2016).
21. F. Arnold, *et al.*, *Nature communications* **7** (2016).
22. B. Q. Lv, *et al.*, *Phys. Rev. X* **5**, 031013 (2015).
23. H. Inoue, *et al.*, *Science* **351**, 1184 (2016).
24. M. D. Bachmann, *et al.*, *arxiv.org* (2017).

25. R. B. Laughlin, *Physical Review Letters* **50**, 1395 (1983).
26. D. Shoenberg, *Magnetic oscillations in metals*, Cambridge monographs on physics (Cambridge University Press, 1984).
27. A. Pippard, *Philosophical Magazine* **46**, 1104 (1955).
28. J. G. Checkelsky, L. Li, N. P. Ong, *Phys. Rev. Lett.* **100**, 206801 (2008).
29. K. Nomura, S. Ryu, D.-H. Lee, *Phys. Rev. Lett.* **103**, 216801 (2009).
30. J. Jung, A. H. MacDonald, *Phys. Rev. B* **80**, 235417 (2009).
31. S. Uji, J. Brooks, Y. Iye, *Physica B: Condensed Matter* **246**, 299 (1998).
32. R. Chambers, *Proceedings of the Physical Society of London Section A* **65**, 458 (1952).
33. A. Abrikosov, *Fundamentals of the Theory of Metals* (Elsevier Sciences Publishers, 1988).
34. K. Brugger, *Journal of Applied Physics* **36**, 759 (1965).
35. A. Suslov, *et al.*, *Review of scientific instruments* **77**, 035105 (2006).

Acknowledgments

E.D.B, F.R., and R.D.M. acknowledge funding from the LDRD program. B.J.R. acknowledges funding from the LDRD-ECR program. M.K.C. acknowledges funding from the U.S. Department of Energy Office of Basic Energy Sciences Science at 100 T program. B.J.R. and R.D.M. conceived of the experiment, E.D.B., N.J.G., and F.R. grew the samples, B.J.R. and R.D.M. performed the focused ion beam lithography, B.J.R., J.B.B., A.M., F.B., and R.D.M. designed and built the experiment, B.J.R., K.A.M., P.J.W.M., M.K.C., J.B.B., and R.D.M. performed the

experiment, B.J.R. and K.A.M. analyzed the data, and B.J.R., K.A.M., A.S., and R.D.M. wrote the manuscript with input from all coauthors.

Supplementary materials

We used focused ion beam (FIB) lithography to prepare single crystal samples of TaAs for high field transport measurements. This allows for careful control over the electrical contact geometry to avoid the effects of inhomogeneous current pathing (see Figure 1). FIB also allows for the production of samples with high geometric aspect ratios, enhancing the resistance to obtain sufficiently large signals in the pulsed field environment.

We discuss the effects of surface degradation due to the FIB process in Figure 2.1. As noted in the main text, ρ_{zz} appears to be activated in temperature above 50 tesla: we fit the conductivity to a simple model to extract a background plus a gap that increases with magnetic field (Figure 2.3).

In addition to the *u*-shaped sample shown in the main text a second ρ_{zz} sample was fashioned and this data is shown in Figure 3. A Hall bar was fashioned to check that the net carrier type in TaAs remains electron-like at all fields: the data is shown in Figure 2.2.

Further information about the pulse-echo ultrasound technique employed here is described in Figure 4, as well as full a data set of the sound velocity from 0 to 65 tesla.

1 Negative Magnetoresistance

Negative magnetoresistance has been reported for a large number of candidate Dirac and Weyl semimetals. The observation of decreasing resistance with increasing magnetic field for $J||B$ has been taken as evidence of an Adler-Bell-Jackiw (ABJ)—or “chiral”—anomaly. Our purpose here is not to dispute all such claims in the literature (since the conditions under which negative magnetoresistance is observed are varied), but rather to highlight a common measurement artifact that can likely explain a large fraction of the reported negative magnetoresistance results.

Semi-classically, magnetoresistance arises from quasiparticle orbits around the Fermi surface in a magnetic field (32, 33). As conductivity is related to the velocity-velocity correlation function averaged over the lifetime of a quasiparticle— $\sigma_{ij} \propto \langle v_i(0) v_j(t) \rangle$ —conductivity is particularly sensitive to cyclotron motion around a Fermi surface. Based on these geometric considerations alone it is entirely expected that, for $B \parallel \hat{z}$, larger magnetoresistance is observed for current perpendicular to the magnetic field (ρ_{xx}) than for current parallel to it (ρ_{zz}). Compensated semimetals have the additional compounding factor that the term linear $\frac{1}{\omega_c \tau}$ in σ_{xy} cancels out, leading to unbounded magnetoresistance in field (33). Thus in a clean compensated semimetal the magnetoresistance anisotropy can increase by several orders of magnitude at high fields, irrespective of whether the bandstructure is “topological” or not (i.e. graphite also exhibits this gigantic anisotropy (7)). Figure 2 of the main text shows that the resistive anisotropy of TaAs is already 100 by 10 Tesla.

The highly anisotropic nature of the magnetoresistance in TaAs means that current injected into the sample through point-like contacts does not necessarily move uniformly through the sample. This effect has been known for quite some time (see page 43 of Pippard (19)), and recently numerical simulations were carried out in the context of experiments on Weyl semimetals by dos Reis *et al.* (20). The result is that the potential drop across a pair of voltage contacts may not reflect the total current injected into the sample, depending on where the contacts are placed. This can be overcome by avoiding point-like contacts and by preparing samples with high aspect ratios with current injection taking place far from the voltage measurement. Even a standard precaution such as contacting the entire ends of a sample to inject current homogeneously does not necessarily produce consistent results since microscopic contact to the sample can still be point like or at the very least inhomogeneous.

To illustrate this point for TaAs we prepared the sample shown in Figure S1. The current path is highlighted in purple; the “good” voltage contacts in red; the “bad” voltage contacts in

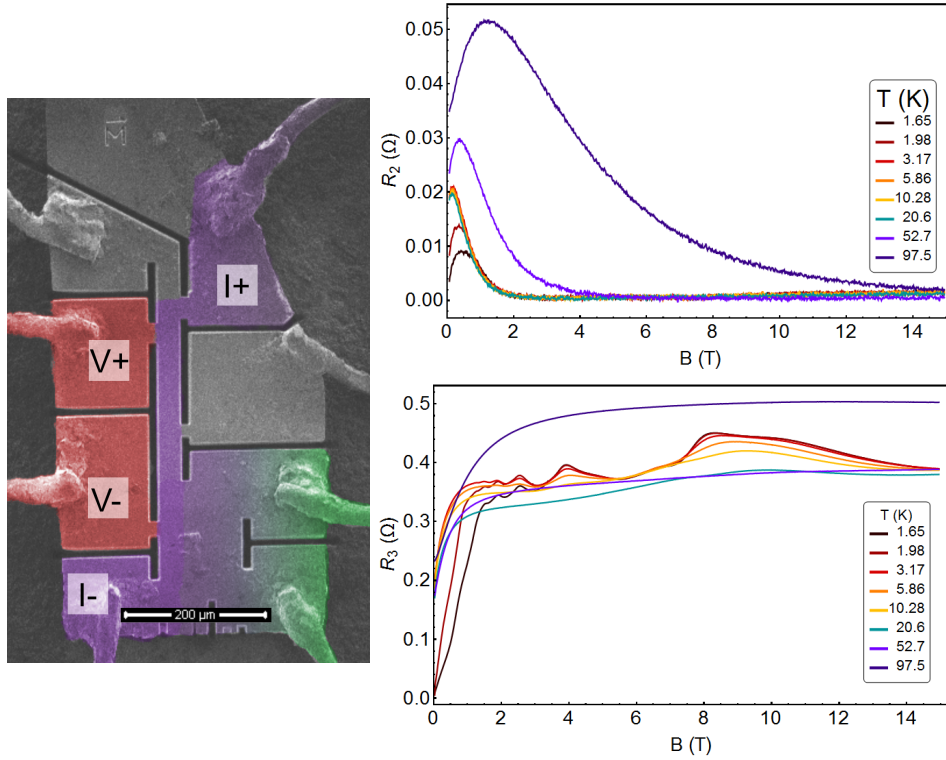


Figure S1: **Demonstration of artificial negative magnetoresistance in TaAs.** *Left:* Single crystal TaAs prepared through focused ion beam lithography to demonstrate the effects of inhomogeneous current paths. The current is injected along the purple path: the voltage is measured at the red contacts—near the current path—and at the green contacts—away from the current path. The crystalline \hat{c} -axis points along the current path: we applied B along this direction as well. *Upper right:* Apparent resistance measured at the contact pads shaded in green. A large negative magnetoresistance is observed at low fields: at high fields no voltage drop is observable due to the fact that no current travels near the green contacts. *Bottom right:* Contact pads placed along the current path reveal the “intrinsic” resistance of the material: roughly constant background magnetoresistance with quantum oscillations above 1 Tesla, where $\omega_c\tau \approx 1$.

green. The corresponding resistances, or rather the voltage drop across the contacts divided by the nominal current, are shown in the two right hand panels for $B||J||\hat{c}$: the top panel corresponds to the green-shaded contacts offset from the current path; the bottom panel corresponds to the red-shaded contacts that are closer to the current path. It is immediately clear that a sizeable “negative magnetoresistance” is visible for the green contacts at all temperatures, similar in character to that reported as evidence for a chiral anomaly in TaAs by Zhang *et al.* (15) and Huang *et al.* (14). In our exaggerated geometry the voltage drops to near-zero at high fields: clearly an unphysical result. The apparent increase in this effect at higher temperatures is due to the increase in resistance and decrease in resistive anisotropy at higher temperatures: it takes more field to isolate the current from the green voltage contacts at higher temperatures because the resistive anisotropy is lower. The red contacts, on the other hand, show positive magnetoresistance that saturates at approximately 1 Tesla—this is expected as $\omega_c\tau$ reaches 1 near this field value. We used an even more restricted current path geometry for the data presented in the main text, and a second sample with similar current path characteristics shows similar resistivity in Figure 3.

2 Surface conductance and activation fits to the conductivity

Both ρ_{zz} and ρ_{xx} shown in Figure 1 of the main text show signs of saturation at the highest resistance values. We can attribute this to the presence of a parallel conduction channel. There are two possible sources of this conduction channel: the surface states which are known to be present on this material and which have been observed via ARPES (22); and/or an amorphous arsenic-depleted layer induced by the FIB (24).

As can be clearly seen in the inset of Figure 1 in the main text, the FIB prepared samples undergo a superconducting transition at low temperatures and low magnetic field. This is also likely a surface effect: it was recently shown that after FIB microstructuring the related ma-

terial NbAs develops an amorphous arsenic-depleted surface layer, as arsenic is preferentially removed during the FIB process, leaving behind a niobium (or in our case tantalum) rich layer that is superconducting (24). This superconductivity is fully suppressed above 2 tesla and 1.5 kelvin, and thus does not affect the majority of the data presented.

By fitting the high-field conductivity for $\vec{J}||\vec{B}||\hat{c}$ including a surface term we can estimate the size of the activation gap for ρ_{zz} in the bulk of TaAs at high fields.

2.1 Surface conductance

If the parallel conduction is a surface channel then it must be treated as a parallel conductance—not a parallel conductivity. We compute the conductance for both the $J||B$ and $J \perp B$ data via

$$S = \begin{pmatrix} \frac{R_{xx}}{R_{xx}^2 + R_{xy}^2} & \frac{-R_{xy}}{R_{xx}^2 + R_{xy}^2} & 0 \\ \frac{R_{xy}}{R_{xx}^2 + R_{xy}^2} & \frac{R_{xx}}{R_{xx}^2 + R_{xy}^2} & 0 \\ 0 & 0 & \frac{1}{R_{zz}} \end{pmatrix}. \quad (1)$$

As shown in the left panel of Figure S2, S_{zz} saturates at around $0.09 \Omega^{-1}$ at high field. For this sample geometry (see Figure 1 of main text, red contacts) this translates to a sheet resistance of about $0.92 \Omega/\square$ for the $J||B$ geometry. Assuming a weak field and temperature dependence, one can subtract off this conductance and re-invert to obtain the bulk conductivity (middle panel of Figure S2). This procedure only produces qualitatively different results below 4 Kelvin and above 70 Tesla, thus we show only the raw resistivity in the main text.

Overall we find that while the presence of a conducting surface layer changes the shapes of our resistivity curves at high fields, it does not alter any of the features from which we draw our main conclusions: the positions of the quantum limits for the various pockets, the onset of the resistivity increase in ρ_{zz} near 50 Tesla, the temperature dependence of the increase in ρ_{zz} , the lack of a strong increase near 50 Tesla in ρ_{xx} , and the sharp downturn in ρ_{xx} near 80 T below 4 K. The consistency of the ultrasound with the features in the transport provides further

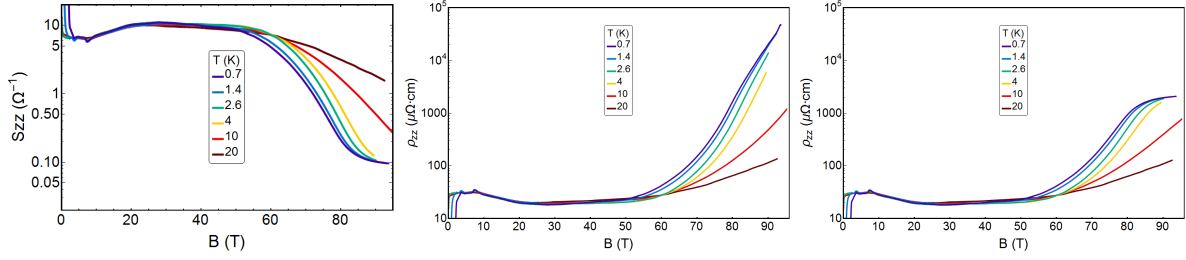


Figure S2: $J||B$ **conductance and resistivity of TaAs**. *Left*: raw conductance of the same sample shown in Figure 1 of the main text on a log scale. *Middle*: resistivity computed once the offset conductance seen in left panel is subtracted off. *Right*: the resistivity from Figure 1 of the main text, including both bulk and surface contributions, reproduced on a log scale. Note that the subtraction only affects the data above ~ 80 Tesla.

confirmation of the intrinsic nature of these features, as there was no FIB lithography performed on the ultrasound sample.

2.2 Hall conductivity

A hall bar was structured to extract both ρ_{xx} and ρ_{xy} from a single measurement by symmetrizing and anti-symmetrizing up and down field pulses (Figure S3). The low-field slope of the Hall produces a net electron density of about 2×10^{18} carriers/cm³, within a factor of two to three of what was reported previously (16). The field evolution of ρ_{xy} in TaAs is remarkably similar to what was reported earlier in graphite (see figure 2 of Uji *et al.* (31)): ρ_{xy} in both graphite and TaAs both increase roughly linearly up to the quantum limit (around 10 tesla for graphite, 36 tesla for the hole pocket in TaAs) and then decrease with increasing field beyond that. We note that at high fields both ρ_{xx} and ρ_{xy} can be contaminated by the surface conductance, and thus statements about the Hall effect that go beyond its sign cannot be made until the surface contribution is either eliminated or quantitatively accounted for.

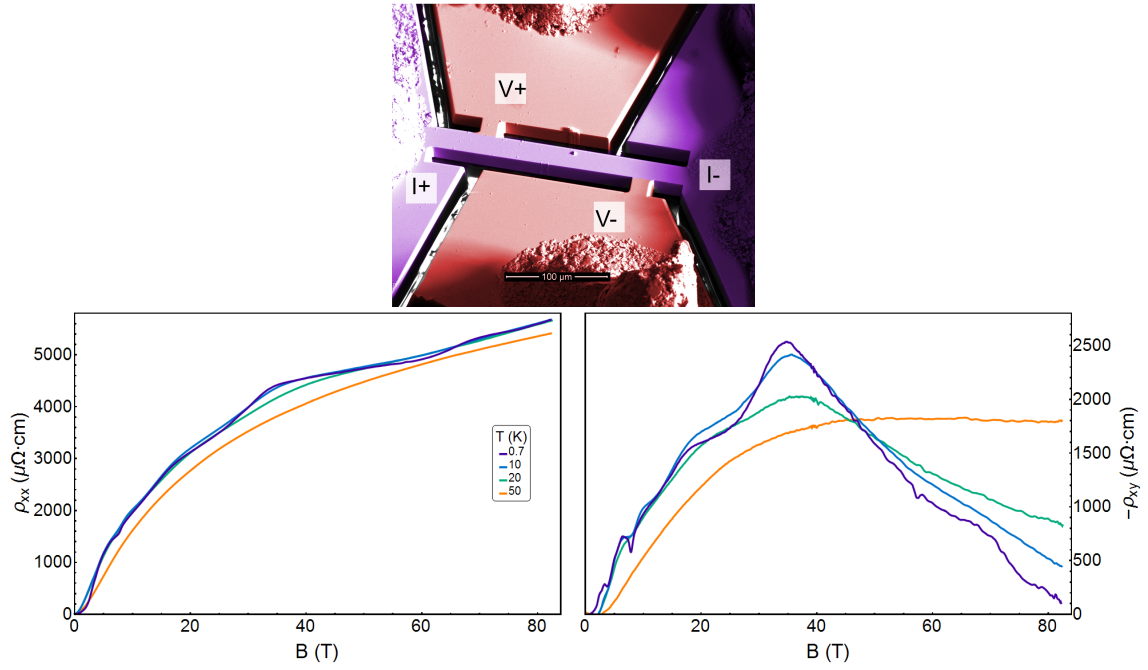


Figure S3: $J \perp B$ resistivity for TaAs. *Top panel:* Single crystal TaAs structure for Hall measurements. *Bottom left:* Longitudinal resistivity from 0 to 82 tesla for a range of temperatures. *Bottom right:* Transverse resistivity from 0 to 82 tesla at the same temperatures. Data was obtained by symmetrizing and anti-symmetrizing up and down field pulses.

2.3 Activation fits to the conductivity

The conductivity for $\vec{J}||\vec{B}||\hat{c}$ takes on an activated form above approximately 50 tesla, and the activation barrier appears to increase with increasing magnetic field. There is also, however, an inherent field and temperature dependence to the conductivity that makes the extraction of any gap difficult without a detailed model of the conductivity. We therefore fit the conductivity $\sigma_{zz}(=1/\rho_{zz})$ at each field slice as a function of temperature to simple mode: a background σ_b plus an activated component

$$\sigma_{zz} = \sigma_b + \sigma_0 e^{-\alpha/T}, \quad (2)$$

where α is the gap in units of kelvin. These fits plus the field-dependent fit parameters are shown in Figure S4.

The background conductivity σ_b (Figure S4a) decreases with field up to about 80 tesla where it is small and weakly field dependent. This supports the idea that at the very highest fields ρ_{zz} is dominated by conductance from an amorphous surface layer. The coefficient of the gapped conductivity σ_0 (Figure S4b) decreases slightly to 80 tesla and then flattens out, suggesting a constant population of carriers that is being gapped out with magnetic field. It is difficult to tell the difference between the Lifshitz-Kosevich amplitude factor for quantum oscillations and an activated gap without a more detailed temperature dependence. We do note, however, that both ρ_{xx} and the sound velocity show a feature that is symmetric about 65 tesla, while ρ_{zz} is qualitatively different in that it rises monotonically. This allows us to rule out a quantum oscillation as the source of the activated behaviour in ρ_{zz} .

3 Second TaAs ρ_{zz} sample

A second TaAs sample (sample 2) in the $\vec{J}||\vec{B}||\hat{c}$ geometry was constructed to reproduce high field features in ρ_{zz} . This sample, shown in Figure S5, is actually the same as shown in Figure

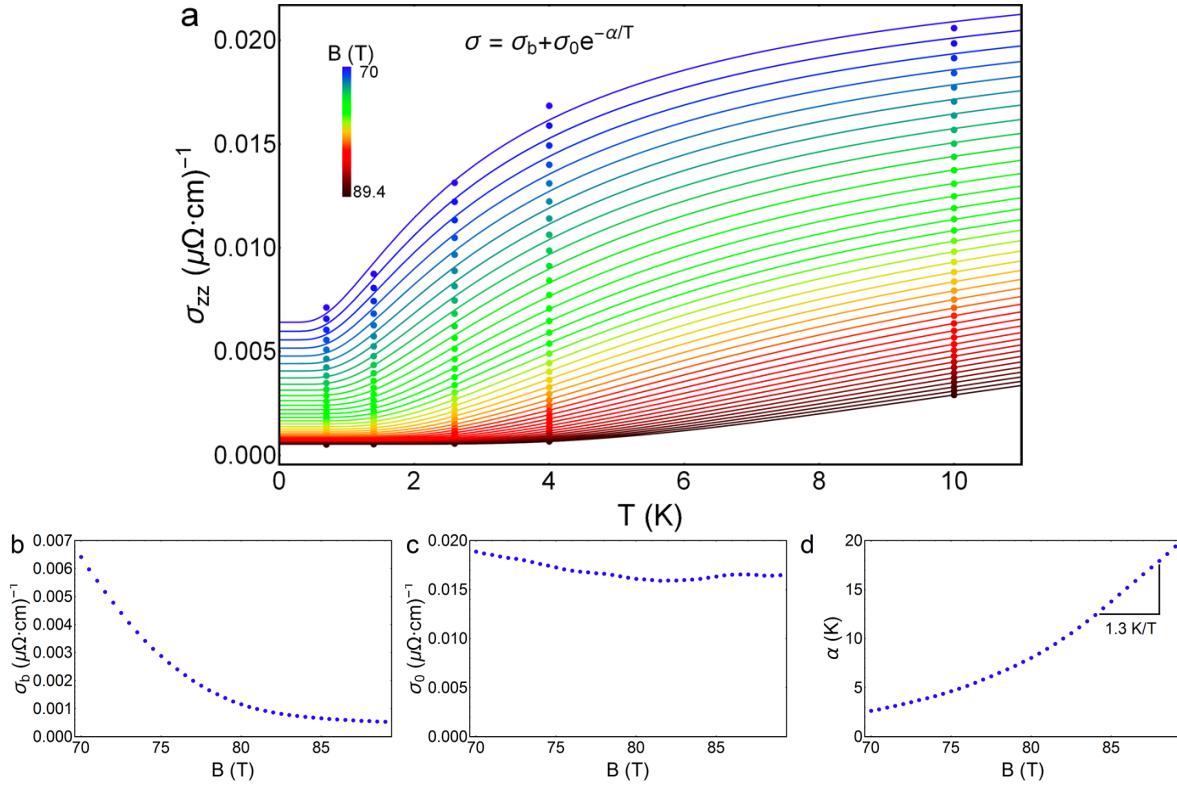


Figure S4: **Fits to σ_{zz} as a function of temperature for different magnetic field values.** **a**, The data shown in Figure 1a of the main text was fit as a function of temperature for different fixed field values between 70 and 90 tesla (the highest field where data at all temperatures is available). **b**, The background conductivity from the fits in **a**. The background saturates above 80 tesla. **c**, the coefficient of the gapped conductivity, which decreases until 80 tesla at which point it remains relatively constant. **d**, The gap coefficient extracted from the fits increases with one slope to around 80 tesla, then increases faster above 80 tesla. The gap opens at a rate of 1.3 kelvin/tesla at high fields.

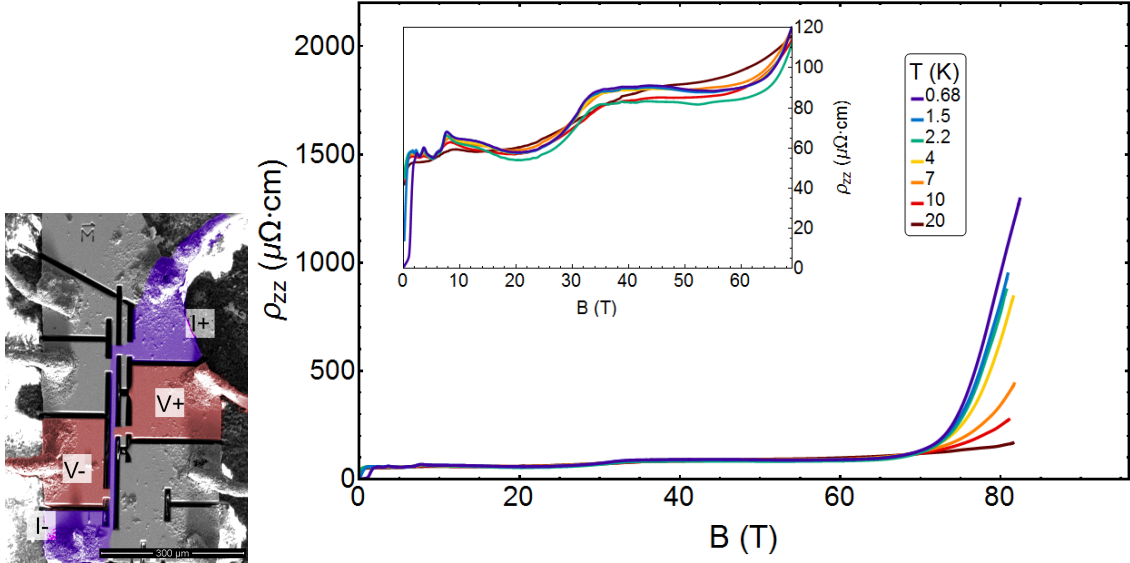


Figure S5: $J||B$ resistivity for TaAs sample number 2. *Left*: the same sample shown in Figure S1 but with the current path (purple) restricted further, and voltage was measured between the red contacts. *Right*: Resistivity up to 82 Tesla from 0.68 to 20 Kelvin. Most features are qualitatively similar to those in Figure 1 of the main text, barring a more pronounced feature at the ultra-quantum limit of the hole pocket near 36 Tesla.

S1 but with the current path even more restricted.

The ρ_{zz} data in Figure S5 is qualitatively similar to that shown in Figure 1 of the main text (sample 1): both show the quantum limit of the larger Weyl pocket near 7.5 Tesla, both have a nearly field and temperature independent resistivity beyond the ultra quantum limit of the hole pocket at 36 Tesla, and both show the onset of increased resistivity in the 50 to 60 Tesla range (depending on temperature). One crucial difference is that sample 2 has a pronounced hump at 36 Tesla, whereas no hump is visible for sample 1. We attribute this to a difference in angle between the magnetic field and the crystalline \hat{c} -axis for the two samples: based on the positions of the last oscillation for the larger Weyl pocket (7.42 T for S_{zz}^1 vs 7.63 T for sample 2) the angle offset is 15° larger for S_{zz}^2 . While this produces only modest changes in the oscillatory contribution from the Weyl pocket, which has its long axis oriented along the \hat{c}

direction, this has a large effect for the hole pocket whose long axis is 90° rotated to the Weyl pocket (see Arnold *et al.* (16) for the Fermi pocket geometries). This presents an extremely unfavourable curvature factor for observing oscillations when the field is aligned directly along \hat{c} : the oscillatory amplitude of a single pocket scales as $1/|\frac{\partial^2 A}{\partial \kappa^2}|$, where κ is momentum along the field direction and A is the Fermi surface extremal area perpendicular to that direction. Thus when the field is nearest to the \hat{c} direction, $1/|\frac{\partial^2 A}{\partial \kappa^2}|$ is smallest and the oscillations are weakest. Because the hole pocket has an aspect ratio of more than 10:1, a 15° offset can produce a large change in curvature factor (easily a factor of 3 for a mass anisotropy of 10 (26)) and hence a large change in oscillation amplitude from this pocket. Misalignment between the crystal \hat{c} axis and the current path, as well as differences in hole mobilities between the two ρ_{zz} samples, may also play a role in the size of the hole-pocket oscillation at 36 tesla.

4 Pulse echo ultrasound

Elastic moduli are thermodynamic variables that describe the linear relationship between stress and strain in a material. The c_{ij} th modulus can be calculated from the free energy F of a system via

$$c_{ij} = \frac{\partial^2 F}{\partial \epsilon_i \partial \epsilon_j}, \quad (3)$$

where ϵ_i is a strain and i, j are Voigt indices that denote the strain ($1 = xx$, $2 = yy$, $3 = zz$, $4 = yz$, $5 = xz$, $6 = xy$). Because the conduction electrons in a metal are always coupled to the lattice, even subtle changes to the electronic structure across a phase transition can show up as large changes in the curvature of the free energy with respect to strain. Hence elastic moduli are a sensitive probe of the electronic structure, and each elastic modulus (in the correct irreducible representation) probes a separate symmetry channel of the interaction between strain and electronic structure. For most experimentally accessible situations the real elastic moduli are frequency independent. The imaginary elastic moduli, on the other hand, describe the ul-

trasonic attenuation and are related to relaxational processes in the material. These can have a strong frequency dependence when the ultrasonic frequency approaches a relaxation timescale in the system—in particular near a phase transition.

Pulse echo ultrasound measures the speed of sound v transmitted through a sample for a specified sound propagation direction and polarization. Elastic moduli can then be computed via the relation $v = \sqrt{\frac{c}{\rho}}$, although care must be taken when choosing the propagation and polarization directions if the relationship between v and any particular c_{ij} is to be kept simple (see Brugger *et al.* (34)). The measurement typically involves generating a short burst of ultrasound (of order a few hundred nanoseconds to a few microseconds) via a piezoelectric transducer, and then recording the echoes with the same transducer as the sound travels back and forth between the faces of the sample parallel to the transducer face. The phase shift between each successive echo is related to the travel time (and hence sound velocity) of the sound pulse, and the amplitude decay with successive echoes is related to the ultrasonic attenuation.

Our implementation of pulse echo ultrasound was similar to Suslov *et al.* (35) with one notable exception: we forwent the mixing stage and directly recorded the full ultrasonic waveform with a 6 GS/s digitizer card (GaGe EON Express). This has two major advantages: it eliminates a large fraction of the electronics; and it allows the use of digital filtering and lock-in techniques that can be optimized and re-processed after the experiment is completed.

We generated 315 MHz longitudinal ultrasound with a 36° Y-cut LiNbO₃ transducer affixed to a (0, 0, 1) face of a TaAs sample (Figure S6). As both the direction of propagation and the polarization are along \hat{c} , we probe purely the c_{33} elastic modulus in this tetragonal crystal (34). The full field dependence at selected temperatures between 0.55 and 20 Kelvin is shown in Figure S6. The velocity v is calculated from the phase shift ϕ between successive echoes as

$$\Delta v = -2\pi f l \frac{\Delta\phi}{\phi^2}, \quad (4)$$

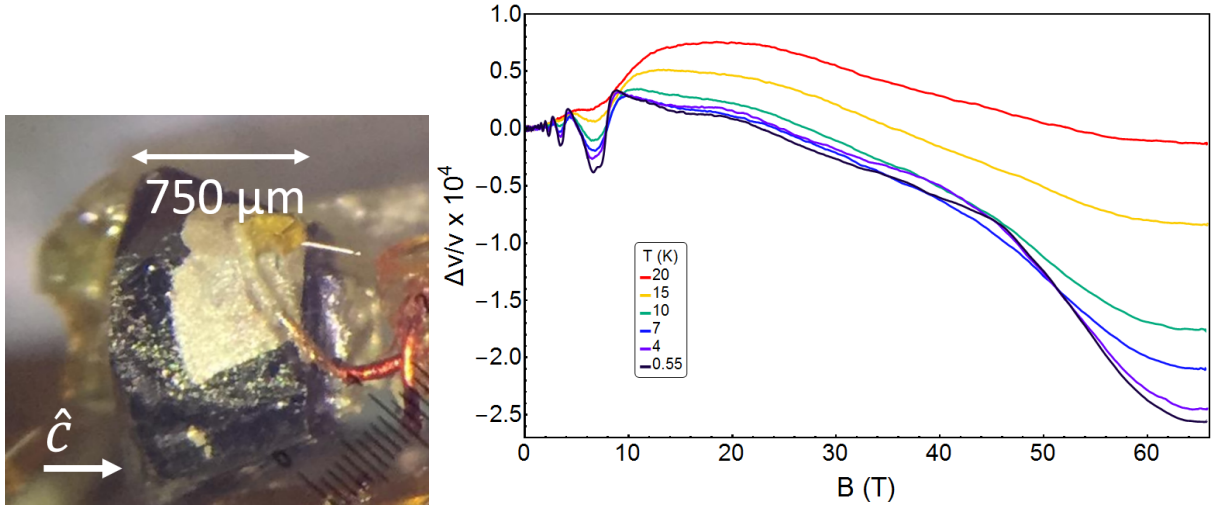


Figure S6: **TaAs sample and ultrasound data from 0 to 65 Tesla.** *Left:* TaAs sample used for ultrasound. Two parallel faces approximately $500 \times 500 \mu\text{m}^2$ were polished perpendicular to the \hat{c} axis. The sample was grounded with silver paint since the backside of the LiNbO_3 transducer was inaccessible. *Right:* Change in sound velocity from 0.55 to 20 K, from 0 to 65 Tesla.

where f is the ultrasonic frequency and l is twice the sample length. The absolute phase ϕ can be obtained from the absolute spacing between successive echoes (a less accurate measure of the sound velocity, but the only way to get the absolute value) via $v = 2\pi fl/\phi$. All plotted velocity shifts are normalized to the phase shift at $B = 0$: the absolute shift as a function of temperature was not obtained.